AVAZ inversion for anisotropy parameters of a fractured medium: A physical modeling study

Faranak Mahmoudian, Gary F. Margrave, Joe Wong, and Brian Russell

ABSTRACT

This report presents an amplitude inversion of PP data, collected through physical modeling, for the Thomsen anisotropy parameters (ϵ, δ, and γ) of an orthorhombic medium. Orthorhombic symmetry, with three mutually perpendicular directions each with different velocity, is the most general symmetry that can describe vertical fractures in horizontal fine layering. Assuming the natural coordinate system along with the fracture orientation, 3D PP data with several azimuths over a phenolic layer have been acquired using the physical modeling facility in CREWES. The phenolic material has been shown to possess orthorhombic symmetry; however it is approximately transversely isotropic with two independent directions. The PP amplitudes picked from the reflection off an isotropic layer and the phenolic layer at several azimuths were used as the data for the inversion. Deterministic amplitude corrections, similar to those used for the real-world acquisition were applied to the physical model amplitudes prior to inversion to scale them to represent the reflectivity. We also applied an additional source-receiver directivity correction specific to the piezoelectric transducers used in the physical modeling. A linearized PP reflection coefficient approximation for an orthorhombic media is used to facilitate the inversion. Some constraints on the vertical velocities and density were also incorporated in the inversion process. Large offset data are required for the azimuthal amplitude inversion of the phenolic layer, as the material shows only slight azimuthal amplitude variations. The results for all three anisotropy parameters from AVAZ inversion compare very favourably to those obtained previously by a traveltime inversion. This result makes it possible to compute the shear-wave splitting parameter, γ, (historically determined from shear-wave data) from a quantitative analysis of the PP reflection data.

INTRODUCTION

Naturally fractured reservoirs hold large hydrocarbon resources and represent attractive economic targets in exploratory ventures. Fractures are defined as cracks in rock that typically have apertures of a few millimeters or less (Gray, 2008). Fracture strike or orientation is the direction of fracture face. The plane parallel to the fractures strike is called isotropic plane and the plane perpendicular to the fractures strike is known as the symmetry plane. It might seem that fracture orientation is random, but measurement confirms a dominant fracture strike related to the major stress direction in the field (Nelson, 2001). Regardless of the origin of the fractures, natural fractures are commonly vertical or near-vertical to the bedding layers. Vertical fractures are impossible to image by seismic with the typical wavelength of tens of meters; however 3D seismic images can provide indirect information about a fractured medium. The dominant orientation of fracture networks makes the fractured medium azimuthally anisotropic for seismic wave propagation; seismic waves travel faster in the direction of the fracture strike. Thus, fractures can be detected by seismic velocity anisotropy.

The azimuthal anisotropy has a strong effect on all seismic wave propagation aspects; it causes shear wave splitting (S-wave birefringence), azimuthally-dependent NMO velocity, and amplitude variation of P- and S-wave reflections with azimuth. Analysis of time delays of split shear waves make it possible to map the orientation and intensity (characterized by the Thomsen anisotropy parameter γ) of a vertical fracture set (Bakulin et al., 2000). In industry practice the shear-wave splitting in three-component seismic has been interpreted directly in terms of the direction of strike of vertical fractures. The azimuthal anisotropy effect on P-wave travel time, appears as azimuthally-dependent NMO and also yields estimates of the ϵ and δ (Tsvankin, 1997b) or a combination of them (η parameter as in Alkhalifah (1997)).

The Amplitude Variation with angle and AZimuth, AVAZ, of the P-wave reflections induced by fractures have been examined in theoretical studies (Daley and Hron, 1977; Thomson, 1988; Rüger, 1997; Bakulin et al., 2000; Vavryčuk and Pšenčik, 1998; Tsvankin and Grechka, 2011), and observed in field seismic (by many authors such as Lynn et al. (1996); Mallick et al. (1998); Perez et al. (1999); Gray (2008)). The difference in seismic Amplitude Variation versus Offset, AVO, responses parallel and perpendicular to fracture strike makes the AVAZ a viable method in analyzing fractures. For a fixed offset (or incident angle), the azimuthal variations of the reflectivity can be approximated by a cosine function, which the reflectivity extremes at the azimuth parallel and perpendicular to fracture strike. The amplitude of this cosine function is commonly interpreted as a measure of the fracture intensity, while the phase gives information about the fracture orientation (Sava and Mavko, 2004). Lynn et al. (1996) and Gray et al. (2002) showed many field examples with good indications from outcrops or FMI logs that the seismic AVAZ fracture analysis is not only detecting the correct orientation of the fractures, but also is a viable method in estimation of fracture intensity. More quantitative interpretion using AVAZ methods is based on the azimuthal differences in the P-wave AVO gradients; usually the AVO gradient calculated according to Shuey's simplification (Shuey, 1985) of the Zoeppritz equations (the AVO gradient is the slope of the least-square's fit of the reflection amplitude versus $\sin^2\theta$, θ being the angle of incident of the P-wave upon the reflector). Lynn et al. (1996) showed in a field example that the variations in the P-wave AVO gradient with azimuth is proportional to to the magnitude of the S-wave birefringence and hence proportion to the fracture intensity.

The anisotropy parameters of a fractured medium are needed for proper seismic imaging of the fractured and underlying layers both at the velocity analysis and the depth migration step. In anisotropic depth migration, the Thomsen anisotropy parameters ϵ and δ are needed in the calculation of travel times for compressional PP data; the parameter γ is used in imaging converted PS data. Anisotropic depth migration makes significant improvements in positioning and reflector continuity compared with isotropic algorithms (Vestrum et al., 1999).

The techniques based on the time delay due to shear wave splitting have been used to estimate the anisotropy parameter γ. Previous AVAZ techniques which have been able to qualitatively predict successfully the orientation of the fractures and the fracture intensity; while the analysis of azimuthally-dependent NMO velocity allows estimation of the ϵ and δ parameters. We present an amplitude inversion technique based on the linear P-wave

reflection coefficient for Horizontal Transverse Isotropy, HTI, media by Rüger (2001). The more general linear approximation for arbitrary anisotropic media by Vavryčuk and Pšenčik (1998) is analytically similar the to Rüger (2001) equation. Inverting the prestack amplitude for different incident angle angle and azimuth, potentially allows the direct estimation of all three anisotropy parameters (ϵ, δ and γ) from P-wave data. Starting with orthorhombic symmetry that best describes a fracture medium, we will discuss the Vavryčuk and Pšenčik (1998) equations for P-wave reflection coefficient as functions of anisotropy parameters, and the Rüger (2001) equations for HTI media. Using these linear approximations the amplitude of PP reflections will be inverted in a least-squared inversion for the anisotropy parameters.

To evaluate the linear approximations of anisotropy reflection coefficients, we tested the azimuthal amplitude inversion on a physical model data from an orthorhombic model. As an valuable adjunct to numerical modeling, the physical modeling on orthorhombic phenolic laminate is well suited for testing an amplitude inversion as the ambiguities inherent in the field data are absent. Tadeppali (1995) acquired 3D multi-offset, multi-azimuth physical modeling data over a simulated fracture model and qualitatively showed that the P-wave AVO effects along different line orientations can be used to detect fracture zone and fracture orientation. Our model consists of four layers with the top and base layer being water, and the isotropic plexiglas and orthorhombic phenolic in between. We successfully estimated the phenolic anisotropy parameters incorporating P-wave data for several azimuths, and our results compare favorably to the anisotropy parameter previously determined by traveltime analysis.

The elastic properties of phenolic LE (density normalized elastic constants (A_{ij}), as well as the Thomsen-style anisotropy parameters for each principal symmetry plane) have been determined by Mahmoudian et al. (2010) through inversion of measured traveltimes. These elastic properties and anisotropic parameters are given on Tables 5 and 6 in Appendix A. Through anisotropic ray tracing using the A_{ij} with a code written by P.F Daley (available in the CREWES MatLab library), we produced traveltimes through the symmetry planes of phenolic that matched the corresponding measured traveltimes vey closely. The close match between the theoretical traveltimes and the observed traveltimes confirmed the accuracy of the elastic constants A_{ij} obtained through inversion.

ORTHORHOMBIC SYMMETRY

Vertical fractures in horizontal fine layering forms an equivalent orthorhombic medium (Schoenberg and Helbig, 1997), see Figure 1. Orthorhombic symmetry is one of the seven classes of the crystal symmetry systems, and is distinguished by three mutually orthogonal planes of mirror symmetry with three distinct directions. One of the symmetry planes in this case is horizontal, while the other two are parallel and perpendicular to the fractures (Figure 1). In fact the equivalent orthorhombic model consists of a Vertical Transverse Isotropy, VTI, background medium with a system of aligned vertical cracks (Rüger, 2001). The HTI symmetry, (which is a useful model for studying the first-order influence of azimuthal anisotropy) is just a degenerate case of orthorhombic symmetry. A medium with orthorhombic symmetry is characterized by nine elastic constants C_{ij}. In the cartesian coordinate system associated with the symmetry planes, the matrix of density normalized

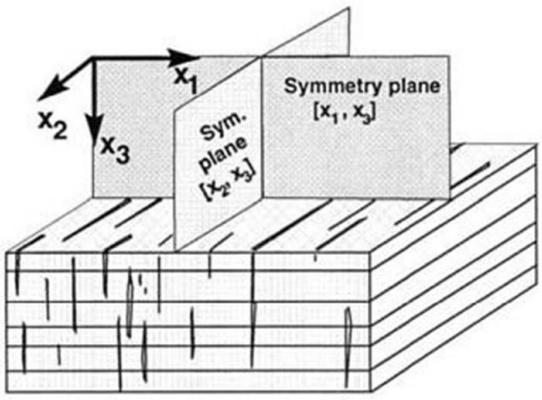

FIG. 1: Orthorhombic model caused by parallel vertical fractures embedded in a finely layered medium (courtesy of Tsvankin (2001)).

elastic constants ($A_{ij} = C_{ij}/\rho$) for orthorhombic symmetry is written in Voigt notation as

$$A_{\alpha\beta} = \begin{bmatrix} A_{11} & A_{12} & A_{13} & & & \\ & A_{22} & A_{23} & & 0 & \\ & & A_{33} & & & \\ & & & A_{44} & & \\ & 0 & & & A_{55} & \\ & & & & & A_{66} \end{bmatrix}. \tag{1}$$

The three P-wave velocities along principal axes determine A_{ii} $(i = 1 : 3)$; the three S-wave velocities also along the principal axes determine A_{ii} $(i = 4 : 6)$. For example $A_{11} = {V_{11}}^2$ and $A_{44} = {V_{23}}^2$. The off diagonal A_{ij} are more than just a combinations of diagonal elements and are dependent to the anisotropy of the medium. To quantify the anisotropy of an orthorhombic medium, we follow Tsvankin (1997a) using the dimensionless generic Thomsen-style parameters ϵ, δ, and γ. For orthorhombic symmetry the anisotropy parameters are defined individually in each symmetry plane; for example they are called $\epsilon^{(2)}$, $\delta^{(2)}$, and $\gamma^{(2)}$ in the symmetry plane (x_1, x_3) normal to the x_2-axis. Table 1 summarizes the relation between elastic constants and these generic Thomsen-style parameters; the relations are valid for any strength of anisotropy.

Table 1: The relationship between elastic constants to the Thomsen-style anisotropy parameters used by Rüger for an orthorhombic medium.

Thomsen parameter	ϵ	γ	δ
(x_2, x_3) plane	$\epsilon^{(1)} = \frac{A_{22}-A_{33}}{2A_{33}}$	$\gamma^{(1)} = \frac{A_{66}-A_{55}}{2A_{55}}$	$\delta^{(1)} = \frac{(A_{23}+A_{44})^2-(A_{33}-A_{44})^2}{2A_{33}(A_{33}-A_{44})}$
(x_1, x_3) plane	$\epsilon^{(2)} = \frac{A_{11}-A_{33}}{2A_{33}}$	$\gamma^{(2)} = \frac{A_{66}-A_{44}}{2A_{44}}$	$\delta^{(2)} = \frac{(A_{13}+A_{55})^2-(A_{33}-A_{55})^2}{2A_{33}(A_{33}-A_{55})}$
(x_1, x_2) plane	$\epsilon^{(3)} = \frac{A_{22}-A_{11}}{2A_{11}}$	$\gamma^{(3)} = \frac{A_{44}-A_{55}}{2A_{55}}$	$\delta^{(3)} = \frac{(A_{12}+A_{66})^2-(A_{11}-A_{66})^2}{2A_{11}(A_{11}-A_{66})}$

Next we examine the linear approximations to the PP reflection coefficient for an interface separating two weakly orthorhombic media.

Table 2: The anisotropic parameters used by Vavryčuk and Pšenčik (1998). The ϵ and γ are equal to the those used by Rüger, while the δ are linearized approximations of the Rüger's δ.

Thomsen parameter	ϵ	γ	δ
(x_2, x_3) plane	$\epsilon^{(1)} = \frac{A_{22}-A_{33}}{2A_{33}}$	$\gamma^{(1)} = \frac{A_{66}-A_{55}}{2A_{55}}$	$\delta^{(1)} = \frac{A_{23}+2A_{44}-A_{33}}{A_{33}}$
(x_1, x_3) plane	$\epsilon^{(2)} = \frac{A_{11}-A_{33}}{2A_{33}}$	$\gamma^{(2)} = \frac{A_{66}-A_{44}}{2A_{44}}$	$\delta^{(2)} = \frac{A_{13}+2A_{55}-A_{33}}{A_{33}}$
(x_1, x_2) plane	$\epsilon^{(3)} = \frac{A_{22}-A_{11}}{2A_{11}}$	$\gamma^{(3)} = \frac{A_{44}-A_{55}}{2A_{55}}$	$\delta^{(3)} = \frac{A_{12}+2A_{66}-A_{33}}{A_{33}}$

LINEAR APPROXIMATION FOR THE PP REFLECTION COEFFICIENTS

In general, the exact reflection coefficients for plane waves given by the Zoeppritz equations are very complicated even for isotropic media, and the dependence of the coefficients on the medium parameters and on incident angle are not linear. They can be expressed in simpler terms if an approximate linearized form is used. There are linearized approximations for the reflection coefficient with respect to changes in medium parameter for both isotropic and anisotropic medium. The linear Aki and Richards (1980) approximation for P-wave reflection coefficient is

$$R_{PP}^{iso}(\theta) = \frac{1}{2\cos^2\theta}\frac{\Delta\alpha}{\bar{\alpha}} - \frac{4\beta^2}{\alpha^2}\sin^2\theta\frac{\Delta\beta}{\bar{\beta}} + \frac{1}{2}\left(1 - \frac{4\beta^2}{\alpha^2}\sin^2\theta\right)\frac{\Delta\rho}{\bar{\rho}}, \tag{2}$$

where θ is the incident angle, α, β are the P- and S-wave velocities, ρ is density, ($\bar{\alpha}$,$\bar{\beta}$,$\bar{\rho}$) are the average values, and ($\Delta\alpha$,$\Delta\beta$,$\Delta\rho$) are the difference of the values in the two layers.

For anisotropic media, the reflection coefficients formulas are available in Daley and Hron (1977) in an exact form for VTI media. Approximations for the reflection coefficients are given by Rüger (2001) for HTI media using Thomsen-style anisotropy parameters. Rüger (2001) has also given approximation for PP reflection coefficients in the symmetry planes of orthorhombic media. Vavryčuk and Pšenčik (1998) have derived reflection coefficients for weak contrast interfaces separating two weakly but arbitrary anisotropic media using a different set of anisotropy parameters than Rüger (2001) (their anisotropy parameters are linear approximations of the ones used by Rüger; see Table 2). The Thomsen-style anisotropy parameters are not explicitly used in Vavryčuk and Pšenčik (1998); their anisotropy parameters are a combinations of A_{ij}'s but can be equivalently renamed to the Thomsen-style anisotropy parameters. The renaming of their parameters to the ones used by Rüger's has been done in this report. For HTI media, the Vavryčuk and Pšenčik (1998) results are analytically similar to Rüger's equation. The PP reflection coefficient given by Vavryčuk and Pšenčik (1998) for general weak anisotropy media (their equation 40) can be

written for orthorhombic media as

$$\begin{aligned} R_{PP}(\theta,\varphi) &= R_{PP}^{iso}(\theta) \\ &+ \frac{1}{2}\left[\Delta(\frac{A_{13}+2A_{55}-A_{33}}{A_{33}})\cos^2\varphi\right. \\ &+ \left.\left(\Delta(\frac{A_{23}+2A_{44}-A_{33}}{A_{33}})-8\Delta(\frac{A_{44}-A_{55}}{2A_{33}})\right)\sin^2\varphi\right]\sin^2\theta \\ &+ \frac{1}{2}\left[\Delta\left(\frac{A_{11}-A_{33}}{2A_{33}}\right)\cos^4\varphi+\Delta\left(\frac{A_{22}-A_{33}}{2A_{33}}\right)\sin^4\varphi\right. \\ &+ \left.\Delta\left(\frac{A_{12}+2A_{66}-A_{33}}{A_{33}}\right)\cos^2\varphi\sin^2\varphi\right]\sin^2\theta\tan^2\theta, \end{aligned} \tag{3}$$

where the φ is azimuth angle with x_1-axis, and the θ is the incident angle. Translating to the Thomsen-style anisotropy parameters using Table 2, the PP reflection coefficient becomes

$$\begin{aligned} R_{PP}(\theta,\varphi) &= R_{PP}^{iso}(\theta) \\ &+ \frac{1}{2}\left[\Delta\delta^{(2)}\cos^2\varphi+\left(\Delta\delta^{(1)}-8\left(\frac{\bar{\beta}}{\bar{\alpha}}\right)^2\Delta\gamma^{(3)}\right)\sin^2\varphi\right]\sin^2\theta+ \\ &+ \frac{1}{2}\left[\Delta\varepsilon^{(2)}\cos^4\varphi+\Delta\varepsilon^{(1)}\sin^4\varphi+\Delta\delta^{(3)}\cos^2\varphi\sin^2\varphi\right]\sin^2\theta\tan^2\theta, \end{aligned} \tag{4}$$

where $\alpha^2 = A_{33}$, and $\beta^2 = A_{55}$. Putting equation 2 for R_{PP}^{iso} into equation 4, we can rewrite the orthorhombic PP reflection coefficient of Vavryčuk and Pšenčik (1998) as a linear approximation with respect to all medium parameters (α, β, ρ, ϵ, δ, and γ),

$$\begin{aligned} R_{PP}(\theta,\varphi) &= \left(\frac{1}{2\cos^2\theta}\right)\frac{\Delta\alpha}{\bar{\alpha}} \\ &- \left(\frac{4\beta^2}{\alpha^2}\sin^2\theta\right)\frac{\Delta\beta}{\bar{\beta}} \\ &+ \left(\frac{1}{2}-\frac{2\beta^2}{\alpha^2}\sin^2\theta\right)\frac{\Delta\rho}{\bar{\rho}} \\ &+ \left(\frac{1}{2}\cos^2\varphi\sin^2\theta\right)\Delta\delta^{(2)} \\ &+ \left(\frac{1}{2}\sin^2\varphi\sin^2\theta\right)\Delta\delta^{(1)} \\ &- \left(\frac{4\beta^2}{\alpha^2}\sin^2\varphi\,\sin^2\theta\right)\Delta\gamma \\ &+ \left(\frac{1}{2}\cos^4\varphi\sin^2\theta\,\tan^2\theta\right)\Delta\varepsilon^{(2)} \\ &+ \left(\frac{1}{2}\sin^4\varphi\sin^2\theta\,\tan^2\theta\right)\Delta\varepsilon^{(1)} \\ &+ \left(\frac{1}{2}\cos^2\varphi\sin^2\varphi\sin^2\theta\,\tan^2\theta\right)\Delta\delta^{(3)}. \end{aligned} \tag{5}$$

For an HTI medium in a coordinate-system shown as in Figure 1 where the symmetry axis coincides with the x_1-axis, $\varepsilon^{(1)} = \delta^{(1)} = 0$, and $\delta^{(3)} = \delta^{(2)}$. Hence, from equation 5, the Vavryčuk PP reflection coefficient for two HTI media contrast becomes:

$$\begin{aligned} R_{PP}^{HTI}(\theta,\varphi) &= \left(\frac{1}{2\cos^2\theta}\right)\frac{\Delta\alpha}{\bar{\alpha}} - \left(\frac{4\beta^2}{\alpha^2}\sin^2\theta\right)\frac{\Delta\beta}{\bar{\beta}} + \left(\frac{1}{2} - \frac{2\beta^2}{\alpha^2}\sin^2\theta\right)\frac{\Delta\rho}{\bar{\rho}} \\ &+ \frac{1}{2}\cos^2\varphi\sin^2\theta\left(1+\sin^2\theta\tan^2\theta\right)\Delta\delta^{(2)} \\ &- \left(\frac{4\beta^2}{\alpha^2}\sin^2\varphi\sin^2\theta\right)\Delta\gamma^{(3)} + \left(\frac{1}{2}\cos^4\varphi\sin^2\theta\tan^2\theta\right)\Delta\varepsilon^{(2)}, \end{aligned} \tag{6}$$

where $\Delta\epsilon$, $\Delta\delta$, and $\Delta\gamma$ are the difference of the values in the two HTI layers.

This expression for the PP reflection coefficient is analytically similar to the one derived by Rüger (2001). Equation 6 approximates the incident and azimuth angle dependent PP reflection coefficient of Rüger (2001). The Rüger's expression for the PP reflection coefficient in a HTI medium with the x_1-axis as the symmetry axis is

$$\begin{aligned} R_{PP}^{HTI}(\theta,\varphi) &= \left(\frac{1}{2\cos^2\theta}\right)\frac{\Delta\alpha}{\bar{\alpha}} - \left(\frac{4\beta^2}{\alpha^2}\sin^2\theta\right)\frac{\Delta\beta}{\bar{\beta}} + \left(\frac{1}{2} - \frac{2\beta^2}{\alpha^2}\sin^2\theta\right)\frac{\Delta\rho}{\bar{\rho}} \\ &+ \frac{1}{2}\left(\cos^2\varphi\sin^2\theta + \cos^2\varphi\sin^2\varphi\sin^2\theta\tan^2\theta\right)\Delta\delta \\ &+ \left(\frac{1}{2}\cos^4\varphi\sin^2\theta\tan^2\theta\right)\Delta\varepsilon \\ &+ \left(\frac{4\beta^2}{\alpha^2}\cos^2\varphi\sin^2\theta\right)\Delta\gamma, \end{aligned} \tag{7}$$

where $\alpha^2 = A_{33}$, $\beta^2 = A_{44}$. Note the ϵ, δ and γ here are exactly the $\epsilon^{(V)}$, $\delta^{(V)}$ and γ used in Rüger (2001)

The following considerations between equation 6 (Vavryčk) and equation 7 (Rüger) reveal that these two equations are analytically very similar.

- The Vavryčk anisotropy parameter $\epsilon^{(2)}$ is exactly the same as ϵ used by Rüger.
- The Vavryčk anisotropy parameter $\delta^{(2)}$ good for weak anisotropy is the linear approximation to the δ used by Rüger.
- The Vavryčk anisotropy parameter $\gamma^{(3)}$ is exactly the same as γ used by Rüger.
- The Vavryčk shear-wave velocity $\beta^2 = A_{55}$ corresponds to the vertically propagating SV-wave in (x_1, x_3) plane. The Rüger shear-wave velocity $\beta^2 = A_{44}$ corresponds to the vertically propagating SH-wave in (x_1, x_3) plane.
- The Vavryčk β is equal to $\beta_{Ruger}(1-\gamma)$ for weakly anisotropy

By calculating and plotting numerical values, we can confirm that the Vavryčk and Rüger expressions for the PP reflection coefficient for a boundary separating two HTI media

are almost equivalent. The specific example ued is the plexiglas-phenolic interface, for which the plexiglas is isotropic and phenolic is HTI. The material properties of the plexiglas and phenolic are given in Appendix A. Figure 2 shows results calculated from equations 6 and 7 for three azimuths: $0°$, $45°$, and $90°$. Note that the phenolic material shows only subtle azimuthal and AVA variations that are noticeable for incident angles larger than $30°$. In this study, we use Rüger's equation (equation 7) as the theoretical basis for AVAZ inversion from AVA/AVAZ amplitudes to estimate the anisotropy parameters.

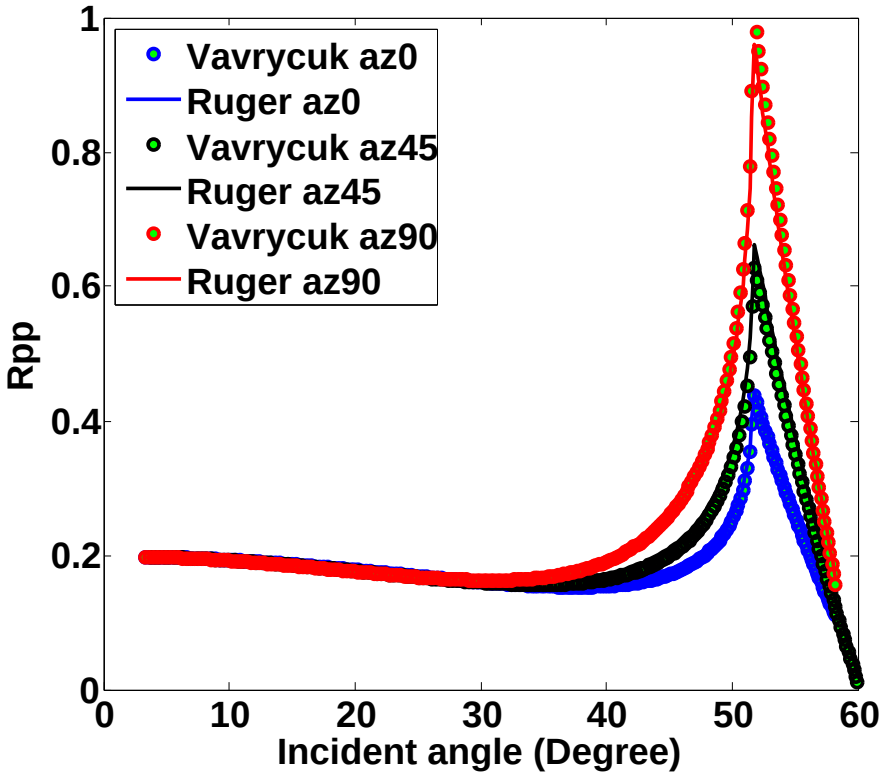

FIG. 2: Comparison of the results from Rüger equation with the Vavryčuk for plexiglas-phenolic interface.

EXTRACTING REFLECTIVITY FROM PHYSICAL MODELING DATA

In physical modeling, seismic data on scaled earth-models are acquired. Our physical modeling experiment has a scale of $(1 : 10000)$ for distance and scale of $(10000 : 1)$ for frequency. Several common-mid-point (CMP) reflection gathers for the azimuths $0°$, $14°$, $27°$, $37°$, $45°$, $53°$, $63°$, $76°$, and $90°$ were acquired over a model consisting of four layers: water, homogeneous plexiglas, homogeneous phenolic LE (which represent the fractured reservoir), and water; a 3D representation of the model is shown on Figure 3. Figures 4 and 5 show the CMP gathers which the seismic profiles are along x_1- and x_2-axis, azimuth $0°$ and $90°$ respectively, with the transducers tip just touching the water surface. Note the azimuth $0°$ profile is collecting data from the symmetry plane, and azimuth $90°$ profile is collecting data from the isotropic plane (fracture plane) of the phenolic layer.

The experiment was shot in water to obtain better quality data for to two main reasons. Firstly it avoids surface waves which mask the reflection data. Secondly the pin transducers

($1.27mm$ in diameter) operated in water are smaller compared to the flat-face transducers ($13mm$ in diameter) used for solid surfaces, and so this mitigates the transducer size issues specific to physical model data. The source and receiver transducer used in this study are piezoelectric pin CA-1136 that utilizes a piezoelectric crystal with $1.27\ mm$ in diameter; as a receiver these transducers act as vertical component geophones. We picked the amplitudes from the experiment where the source and receiver transducers were placed $2\ mm$ beneath the water surface to avoid overlapping the primary and ghost event; Figure 6 shows the CMP gather from a profile along symmetry axis (x_1-axis) with transducers right at the water surface versus data with transducers $2\ mm$ inside the water. More details about the laboratory equipments and set-up used in this study are as described by Wong et al. (2009).

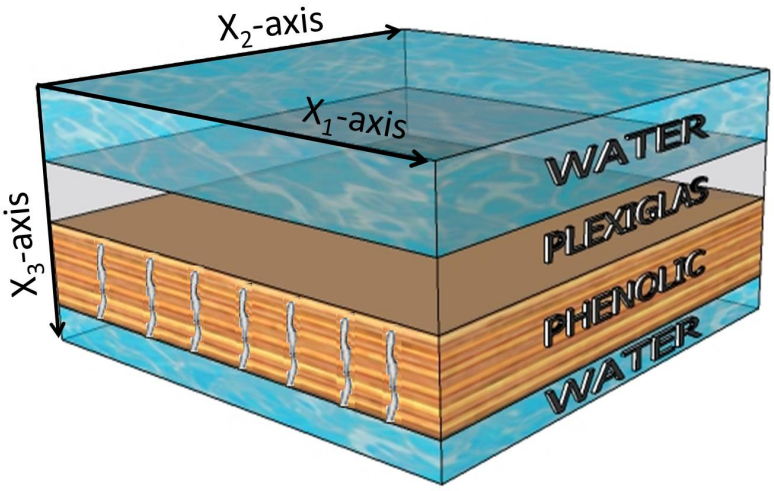

FIG. 3: Four-layer earth model used in physical modeling acquisition. The layers are water, isotropic plexiglas, orthorhombic phenolic, and water.

The AVA, amplitude versus angle, analysis is intensive and involves many details. Its success depends upon correct amplitude compensation for various effects that can mask the AVA information. Field recordings of seismic data do not indicate target reflectivity due to numerous effects. Spratt et al. (1993) counted a variety of effects which disturb seismic amplitudes; among them geometrical spreading, transmission loss and overburden effect, energy partitioning due to free surface, multiple reflections, anelastic attenuation, ground roll, variation in shot strength or receiver coupling, source radiation pattern, receiver array response, geophone response, and thin bed tuning. Such effects may alter amplitudes and are independent of the model properties.

Deterministic amplitude corrections, similar to those used for real-world acquisition and analysis, were applied to the physical model amplitudes prior to inversion to scale them to represent the reflectivity. The corrections for these factors are reviewed in Appendix B. We also applied an additional source-receiver directivity correction specific to the piezoelectric transducers used in the physical modeling. For this study, we have corrected the picked amplitude from plexiglas-phenolic interface for geometrical spreading, emergence angle, free surface, transmission loss, and source-receiver directivity. We examine the source-receiver directivity correction in more detail.

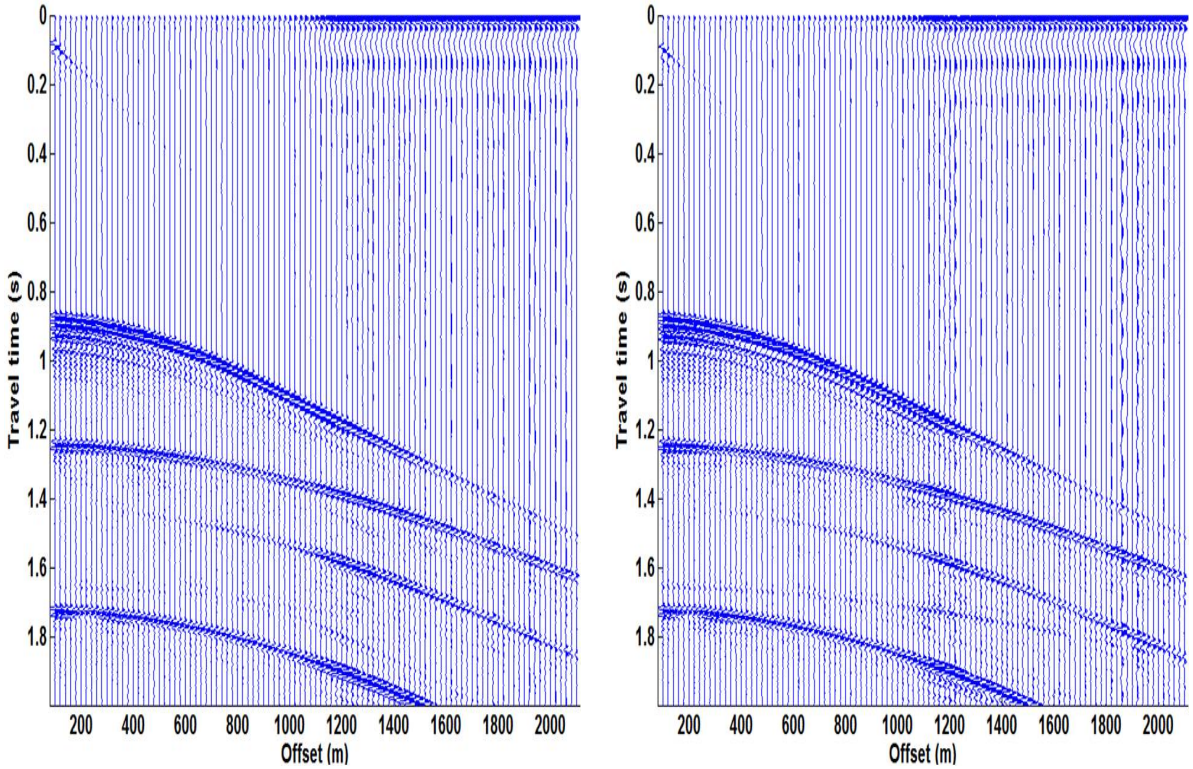

FIG. 4: Physical model vertical-component CMP gather acquired over four-layered model for profiles along x_1-axis (azimuth $0°$) and x_2-axis (azimuth $90°$). Both source and receiver transducer's tips are just touching the water surface. Data has been filtered to [0 80] frequency range, and long-gate automatic gain control has been applied to it.

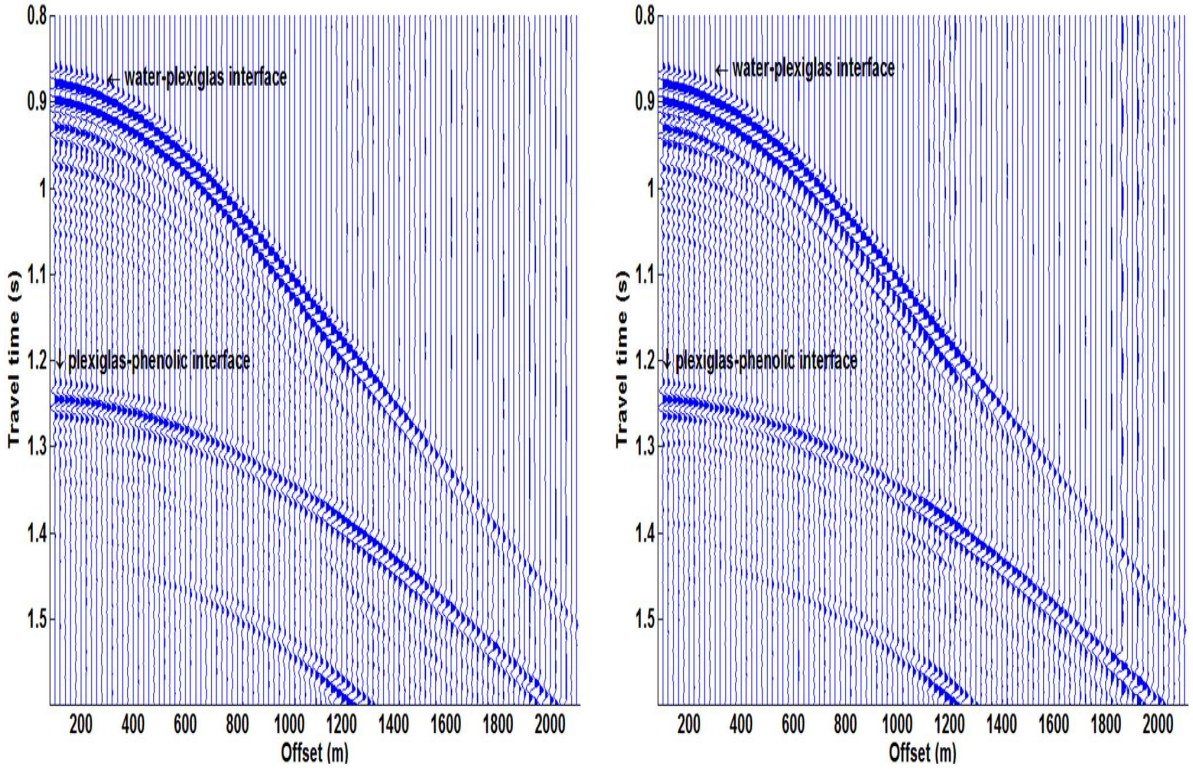

FIG. 5: Zoomed physical model data from azimuth $0°$ and $90°$.

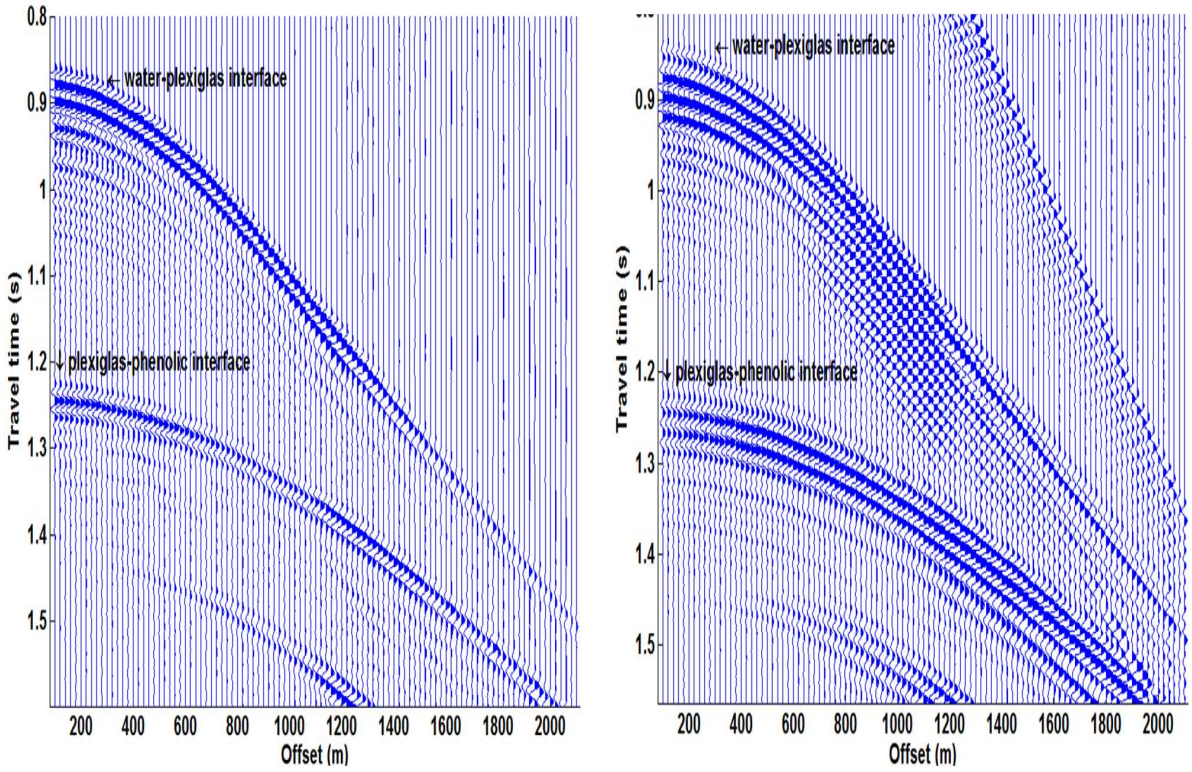

FIG. 6: (left) Physical model vertical-component data from profiles along x_1-axis (azimuth $0°$) with transducers just touching the water surface. (right) With transducer tips $2mm$ below the water surface.

Source-receiver directivity

The source and receiver directivities will affect the offset behaviour of the recorded reflections. Directivity is the property of a piezoelectric transducer that gives its response a pronounced directional bias. Buddensiek et al. (2009) presented an excellent overview of the performance of piezoelectric transducers and their amplitude directivities, in which they examined the transducer responses not only in a physical modeling context, but in general usage. An illustration of a directional circular transducer (similar to what we used in this study) performance is shown in Figure 7. For disc-shaped or circular transducers, the directivity response can be described analytically by the following two equations (Krautkrämer and Krautkrämer, 1986)

$$A = 4A_0 \frac{J_1(X)}{X} \sin\left(\frac{\pi D}{8\lambda z}\right), \tag{8}$$

$$X = \frac{\pi D}{\lambda} \sin\gamma, \tag{9}$$

where A_0 is initial amplitude, D is the effective diameter of the piezoelectric crystal, λ is the wavelength, z is the distance to the emitting plane, γ is the angle to the vertical axis, and J_1 is the Bessel function of order 1. The pressure field (or amplitude) of a circular transducer becomes more directed as the wavelength shortens. For real transducers operating in water, the effective diameter D is determined experimentally by measuring the amplitude at a fixed distance between the source and receiver transducers (Buddensiek et al., 2009). Note that equation 8 is similar to an array response (e.g., 6 in Appendix B). For our measurements, the dominant frequency is $520kHz$. In water, with an acoustic velocity of

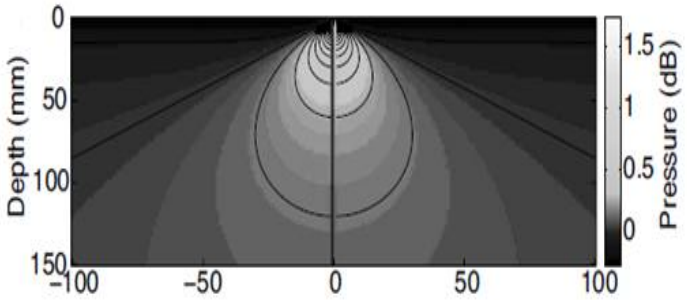

FIG. 7: The calculated pressure field for a circular transducer of diameter $12mm$ as a function of depth and angle for 200 kHZ frequency (courtesy of Buddensiek et al. (2009)).

$1485\ m/s$, the dominant wavelength is $2.86mm$. The directivity corrections calculated for the water-plexiglas reflection amplitudes picked from the $0°$ and $90°$ azimuths using effective diameters D of $1.4mm$ and $1.6mm$, respectively. The corrected amplitudes are shown on Figures 8 and 9, where they are compared with theoretical amplitudes predicted by the spherical-wave and plane-wave Zoeppritz equations (implemented as the JAVA applet Spherical Zoeppritz Explore 3.0 by Ursenbach et al., 2006, and available on the CREWES website). The spherical-wave Zoeppritz predictions are more realistic for our data, since our sources and receivers do not produce and detect plane waves. The figures show, however, that spherical-wave and the plane-wave predictions are virtually identical for incident angles that are less than and not close to the critical angle.

The water-plexiglas reflector amplitudes from the $90°$ data need a slightly larger effective diameter of $1.6mm$ to fit the predicted theoretical reflectivities. The transducers are apparently not quite symmetric in the two azimuth directions $0°$ and $90°$. Another possible explanation is that evaporation had changed the water level slightly between the times of the acquisition of the $0°$ and $90°$ azimuth data, and this also changed slightly the recorded amplitudes. After all the corrections, the water-plexiglas reflector amplitudes for the $0°$ and $90°$ azimuths follow the theoretical spherical Zoeppritz predictions very closely. The picked amplitudes for the other azimuths were corrected for directivity using effective diameters set proportionally between $1.4mm$ and $1.6mm$.

We now address the reflections from our target, the plexiglass-phenolic reflector. First of all, we corrected $90°$ azimuth picked amplitudes for directivity by using an effective diameter of $4.5mm$. This value gave a good fit to the spherical-wave Zoeppritz predictions (the $90°$ azimuth vertical plane is the nearly-isotropic plane for the phenolic layer, and we expect it to follow closely the isotropic spherical Zoeppritz predictions). Between the water-plexiglas reflector and the Plexiglas-phenolic reflector, the ratio of best-fit effective diameters for the $90°$ azimuth is $(4.5mm/1.6mm) = 2.81$. To correct the Plexiglas-phenolic reflected amplitudes for directivity for all the other azimuths, effective diameters given by $D1 = 2.81 \times D0$, where $D0$ is the diameter previously determined for the water-Plexiglas reflector. For example, the effective diameter for the $0°$ azimuth data from the water-Plexiglas reflector is $1.4mm$; the best-fit effective diameter at this azimuth for the Plexiglas-phenolic reflector is thus $2.81 \times 1.4 = 3.94mm$.

The directivity correction given in equation 8 is virtually identical to the directivity

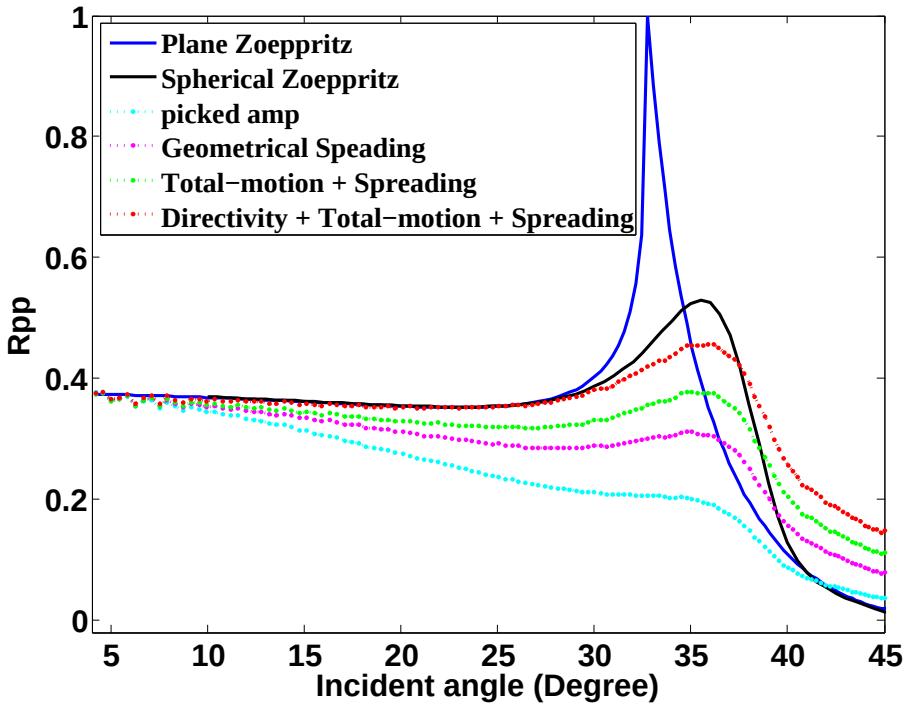

FIG. 8: Azimuth $0°$: water-plexiglas reflector amplitudes corrected for geometrical spreading, emergence angle (total motion), and directivity effects. The effective diameter of $1.4mm$ is used. Note the mismatch beyond critical angle is due to interference by head-wave.

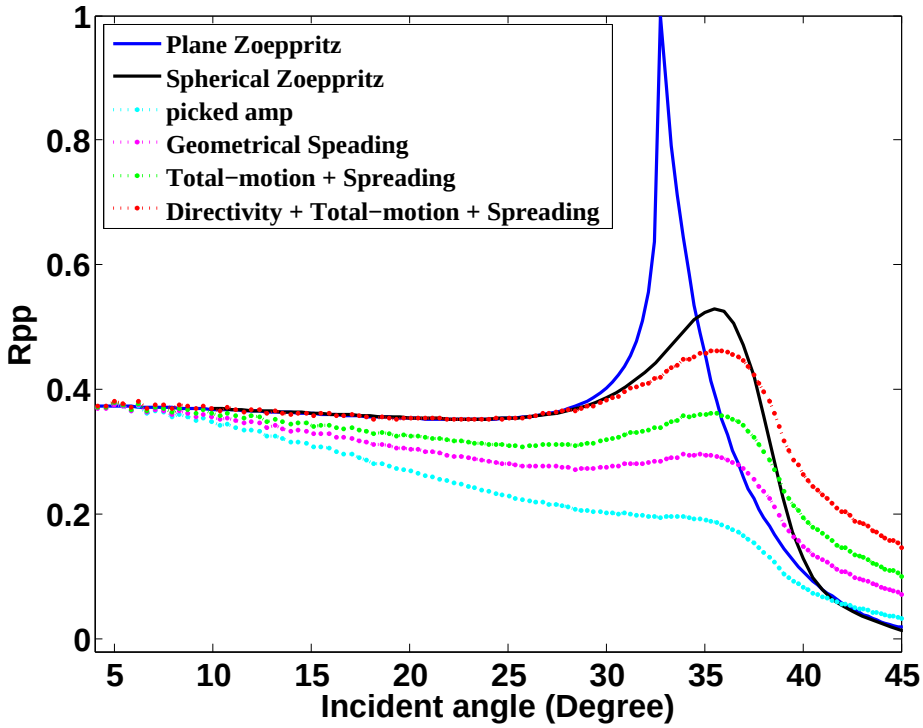

FIG. 9: Azimuth $90°$: water-plexiglas reflector amplitudes corrected for geometrical spreading, emergence angle (total motion), and directivity effects. The effective diameter of $1.6\ mm$ is used.

correction calculated numerically by Wong and Mahmoudian (2011), as is shown by the plots on Figure 10. In the numerical method, the circular face of a disc transducer is divided up into many small elements. Each element acts as a source, and the source Green's functions for isotropic and homogeneous acoustic media from all elements are summed at receiver positions at fixed distance R (large compared to the wavelength and transducer diameter) from the center of the disc, but at different polar angles relative to the symmetry axis of the disc.

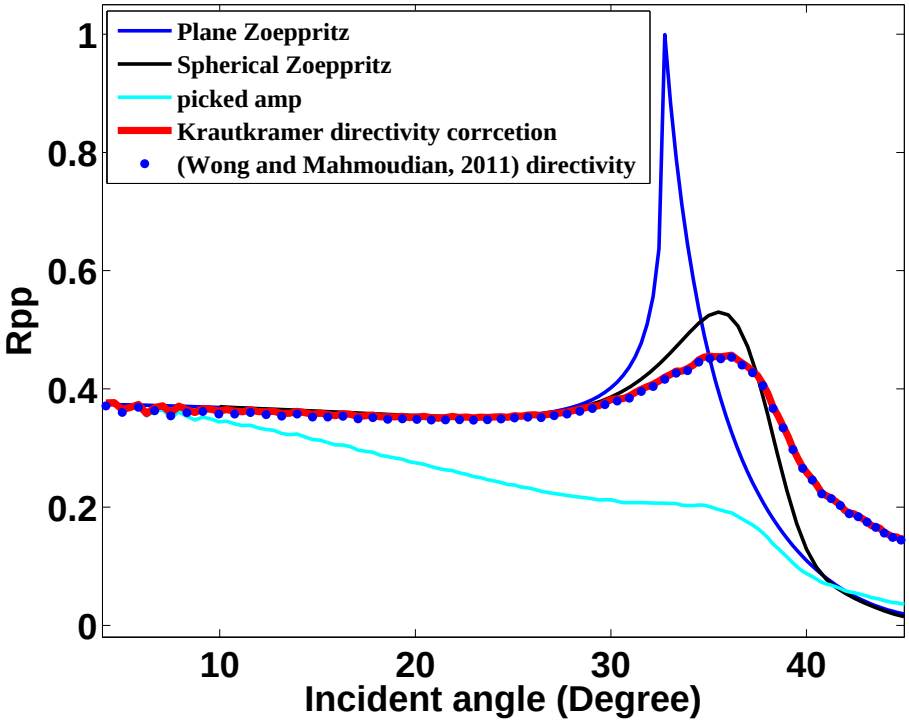

FIG. 10: Azimuth 0° data: directivity correction for water-plexiglas reflector amplitudes using equation 8, and correction by Wong and Mahmoudian (2011); the effective diameter of $1.4mm$ is used for both corrections.

Picking reflection amplitudes

For each CMP gather at each azimuth, the event from the reflecting interface of interest was identified and the arrival times were picked manually. For the water-Plexiglas reflections, the amplitude was picked on the wavelet immediately following each arrival time. For the Plexiglas-phenolic reflection, which was much weaker than water-Plexiglas reflection from a shallower depth, the amplitude was picked on the strongest wavelet following each arrival time. Because the transducers in this study operated near the water surface, all reflections showed a primary and ghosts. To make sure that the primary and the ghost events are not overlapping and damaging the amplitude information required for AVA analysis, we conducted a set of measurements designed to see how the ghosts behaved.

In this new experiment, the source and receiver were kept at a fixed offset of $10mm$, and seismograms were recorded at $0.2mm$ depth intervals as they were both raised from a depth of $10mm$ up to a depth of $0mm$ (at which the active tips of the transducers were nominally even with the water surface). Figure 11 shows the seismograms from this experiment. On

Figure 11, the primary and the ghost for the water-plexiglas reflection are clearly visible at 1 second (two-way travel time). The primary has a time moveout towards earlier times as tip depth increases; this is as expected since, as tip depth increases, the lengths of the raypaths from the tips to reflecting interface decreases. For the ghost, the arrival times increase as tip depth increases; this also is as expected, since the total raypaths for this ghost includes segments from the tips to the surface (lengths increase with tip depth) and segments from the surface to the reflecting interface (lengths are independent of tip depth).

There is a third arrival identified on Figure 11 is XX high-lighted in red, which has almost zero arrival time change as tip depth increases. This arrival behaves as if the source and receiver are both located at the water surface, and therefore there is no apparent change in travel path length as tip depth change. The following scenario provides a possible explanation for this. The body of the source piezopin vibrates up and down simultaneously when the piezoelectric element at its tips is excited by high voltage. At the point where the source piezopin body enter the water, the vertical motion of the body causes a nearby circular area of the water surface (which acts as behaves somewhat like a membrane because of surface tension) to vibrate also in unison. This vibrating ring of water surface behaves as a secondary source whose distance from the reflecting surface is constant regardless of tip depth. By reciprocity, the receiver piezopin has a similar response. What are these "rings of vibrating water surface" that act as a secondary source and a secondary receiver? Figure 12 is a photograph of two piezopins whose tips are just below the water surface. It is quite obvious that a circular meniscus forms around each piezopin.

Thus, we believe the XX reflection arrival on Figure 11 is due to the piezopin contact points with the water surface acting as source and receiver. The XX arrival is stronger than the primary and ghost arrivals, and the best-fit directivity correction associated with requires a large effective diameter (from figure 12, and knowing that the piezopin body near the tips have a diameter of $2.36mm$, we can estimate that the diameter of the menisci are in the range $3mm$ to $6mm$). From this experiment and the data on Figure 11, we chose $2mm$ as the optimal depth for the tips of the source and receiver piezopins. For the plexiglas-phenolic reflection, we picked the strongest wavelets following the arrival times. Since these strongest wavelets are associated with XX arrivals from the menisci, we also chose an effective diameter close to those of the menisci (i.e., in the range $3mm$ to $6mm$).

INVERSION IMPLEMENTATION

The corrected amplitude of the plexiglas-phenolic reflections for nine azimuths between $0°$ and $90°$ are shown in Figure 13. The corrected amplitudes from only $0°$, $45°$, and $90°$ azimuths are shown in Figure 14 to demonstrate more clearly azimuthal amplitude variations. Figure 14 shows small azimuthal amplitude variations due to the orthorhombic phenolic layer. This result was expected as the theoretical predicted reflectivity showed small azimuthal amplitude variations, see Figure 2. On this Figure, we also see that only for incident angles larger than $30°$ are the AVAZ variations noticeable for the plexiglas-phenolic reflection. The physical model amplitudes follow the theoretical predicted reflectivity closely for the incident angles up to the critical angle, see Figure 15.

The corrected amplitudes of the plexiglas-phenolic reflector represent the experimental

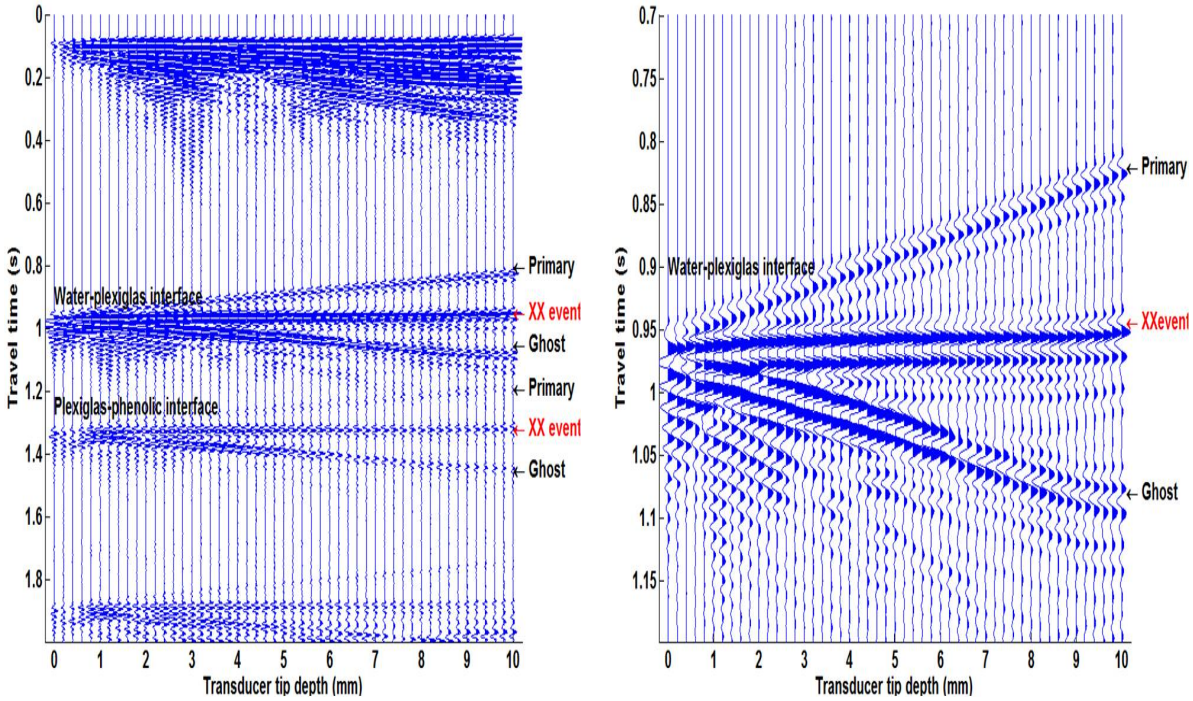

FIG. 11: (left) Physical model data acquired at a single source-receiver offset of $10mm$ with different transducer depths in water. (right) Zoomed on times for the water-plexiglas reflection.

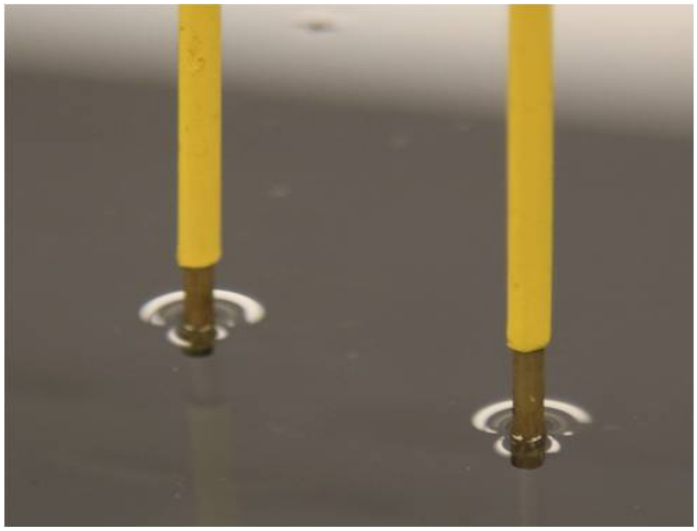

FIG. 12: Water meniscus generated at the transducers contact with water.

reflectivity and will be the input data for the AVAZ analysis. We note that the deterministic amplitude corrections are only approximate, so the corrected amplitude still might not represent reflectivity perfectly.

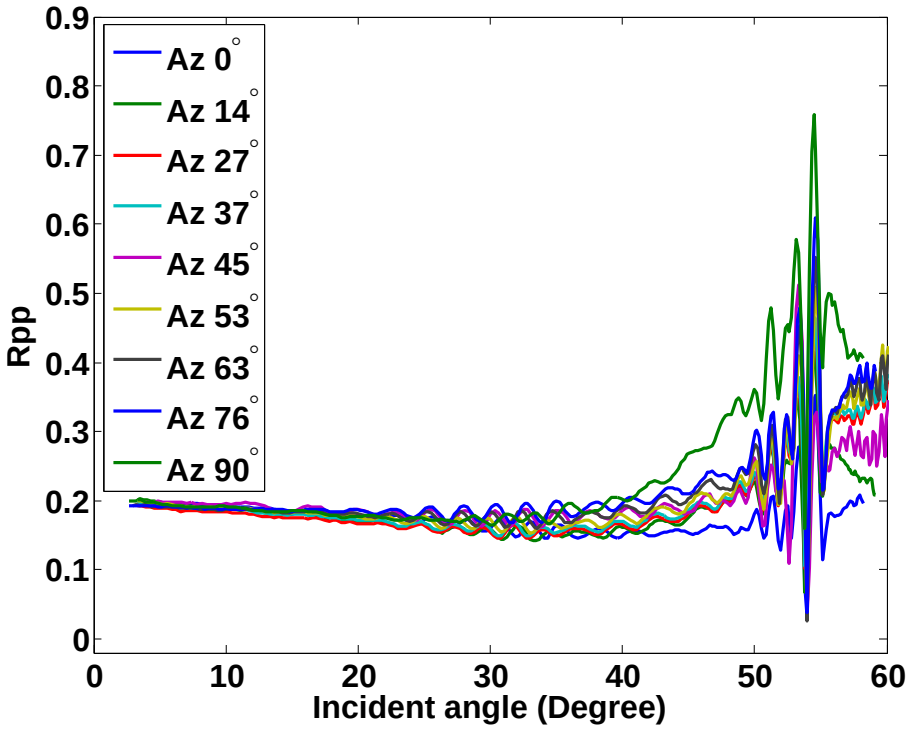

FIG. 13: (left) Corrected amplitudes of plexiglas-phenolic reflector picked from azimuths $0°$, $14°$, $27°$, $37°$, $45°$, $53°$, $63°$, $76°$, and $90°$ versus incident angle.

In the theory section we started with orthorhombic symmetry as the HTI is only a good first approximation for azimuthal anisotropy, just to show that the PP reflection coefficient in orthorhombic media could be as easily as Rüger's equations for HTI media. However since the the phenolic is close to an HTI medium, we will use the Rüger's expression (equation 7) as the basis for our AVAZ inversion. We write equation 7 in a simpler way as

$$R = A\frac{\Delta\alpha}{\bar{\alpha}} + B\frac{\Delta\beta}{\bar{\beta}} + C\frac{\Delta\rho}{\bar{\rho}} + D\,\Delta\delta + E\Delta\varepsilon + F\Delta\gamma, \tag{10}$$

where R is the PP amplitude, and the coefficients A, B, C, D, E, and F are expressed in detail on equation 7. Incorporating the amplitudes of plexiglas-phenolic reflection from profiles along the azimuths $0°$, $14°$, $27°$, $37°$ $45°$, $53°$, $63°$, $75°$ and $90°$ for different incident angles up to $40°$ as the input data (R_{mn}), the linear equation 10 can be used to express a linear system of n equations with six unknowns:

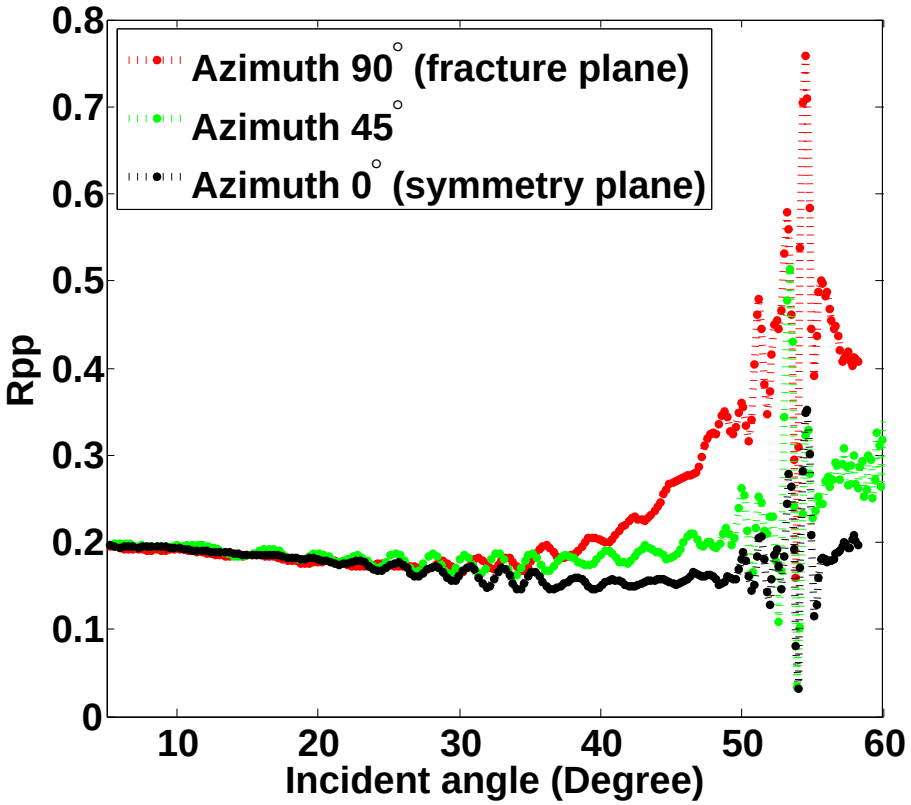

FIG. 14: Azimuth 0°, 45°, and 90° plexiglas-phenolic corrected amplitude.

$$\begin{bmatrix} A_{1\varphi_1} & B_{1\varphi_1} & C_{1\varphi_1} & D_{1\varphi_1} & E_{1\varphi_1} & F_{1\varphi_1} \\ \vdots & \vdots & \vdots & \vdots & \vdots & \vdots \\ A_{n\varphi_1} & B_{n\varphi_1} & C_{n\varphi_1} & D_{n\varphi_1} & E_{n\varphi_1} & F_{n\varphi_1} \\ \vdots & \vdots & \vdots & \vdots & \vdots & \vdots \\ \vdots & \vdots & \vdots & \vdots & \vdots & \vdots \\ A_{1\varphi_m} & B_{1\varphi_m} & C_{1\varphi_m} & D_{1\varphi_m} & E_{1\varphi_m} & F_{1\varphi_m} \\ \vdots & \vdots & \vdots & \vdots & \vdots & \vdots \\ A_{n\varphi_m} & B_{n\varphi_m} & C_{n\varphi_m} & D_{n\varphi_m} & E_{n\varphi_m} & F_{n\varphi_m} \end{bmatrix}_{(nm\times 6)} \begin{bmatrix} \Delta\alpha/\alpha \\ \Delta\beta/\beta \\ \Delta\rho/\rho \\ \Delta\delta \\ \Delta\varepsilon \\ \Delta\gamma \end{bmatrix}_{(6\times 1)} = \begin{bmatrix} R_{11} \\ \vdots \\ R_{n1} \\ \vdots \\ R_{1m} \\ \vdots \\ R_{nm} \end{bmatrix}_{(nm\times 1)} \tag{11}$$

where $m = 9$ is the number of azimuths, and n is the number of incident angles. Or, in matrix form,

$$G_{(nm\times 6)} m_{(6\times 1)} = R_{(nm\times 1)}. \tag{12}$$

The unknown vector m will result from a damped least-squares inversion, as $m = (G^T G + \mu)^{-1} R$ and the μ is the damping factor.

In this implementation of the amplitude inversion, we try to estimate simultaneously all six parameters α, β, ρ, δ, ϵ, and γ, Figure 16 shows that this AVAZ inversion gives reasonable results for α, ρ, δ, and ϵ, but not for β, and γ. These two parameters are related to PS and SH data. The above six-parameter inversion was not very stable due to the three

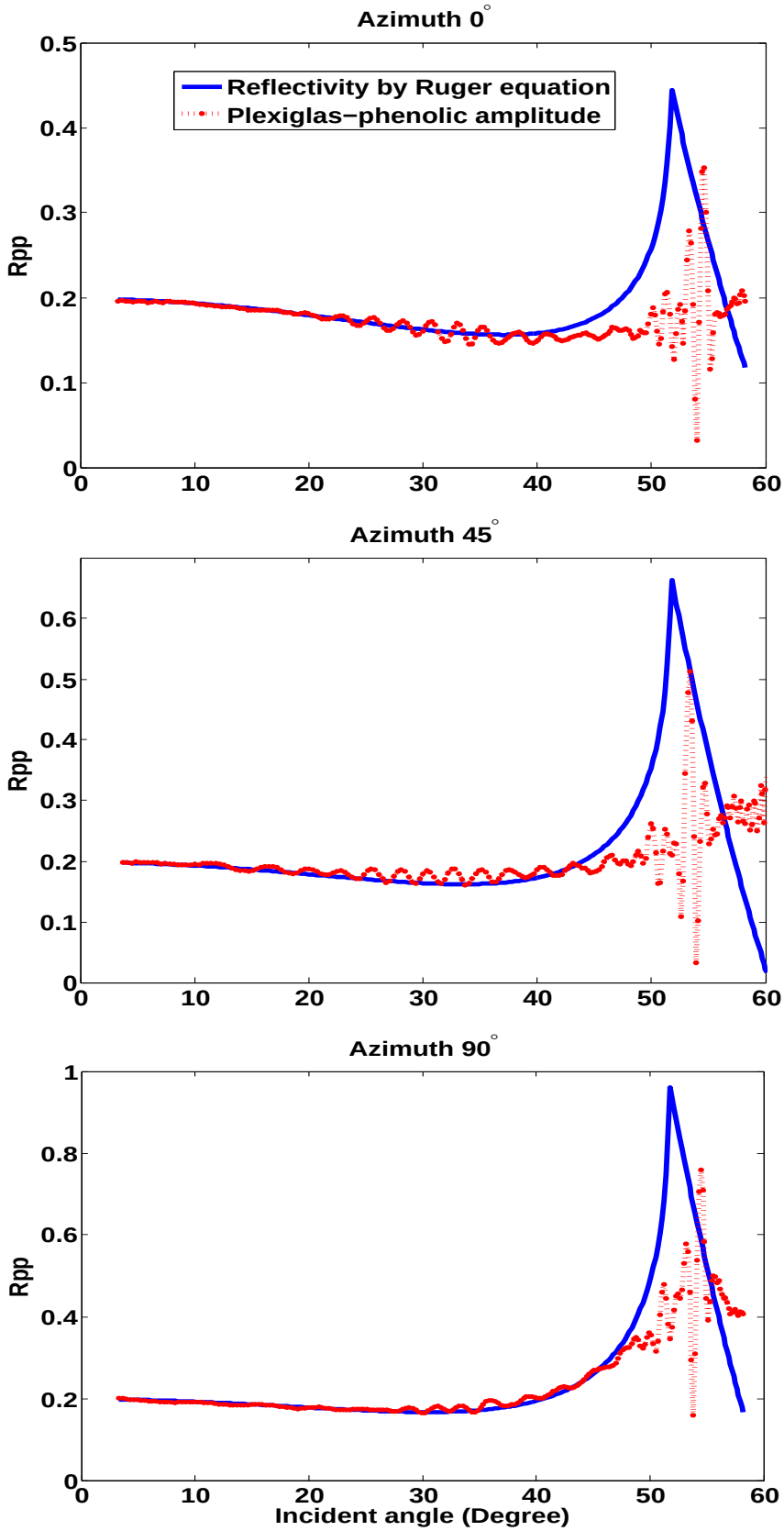

FIG. 15: Comparing measured reflected amplitudes from the plexiglas-phenolic interface with the plane-wave PP reflectiviy predicted by the Rüger's equation. The corrected measured amplitude's follow the theoretically predicted reflectivity closely for incident angles up to the critical angle.

very small singular values in inverting the matrix G. Data from incident angles less than 40° were used in the inversion, but incorporating data from larger angles would introduce larger errors to the inversion because of our using a linearized equation 12. Still the result is not disappointing as the theoretical AVAZ effect for the plexiglas-phenolic reflection is small to begin with.

In an effort to stabilize the inversion, we applied some constraints to the first three variables, $\Delta\alpha/\alpha$, $\Delta\beta/\beta$, and $\Delta\rho/\rho$. Also, there are many other methods available for inverting for vertical P- and S-wave velocity and density such as AVA inversion or incorporating well log information. In order to put some constraints on the first three variables, we used the azimuth 90° data to invert for $\Delta\alpha/\alpha$, $\Delta\beta/\beta$, $\Delta\rho/\rho$, as the azimuth 90° is our isotropic plane. Figure 17 shows the error of estimating the first three parameters from azimuth 90° data. These estimations of $\Delta\alpha/\alpha$, $\Delta\beta/\beta$, $\Delta\rho/\rho$ are used to constrain the AVAZ inversion for anisotropy parameters ϵ, δ, and γ. Figure 18 show the inversion results for the anisotropy parameters ϵ, δ, and γ. With this constraint we included data from slightly higher incident angle (up to 43°). With this constrain the inversion results for δ, ϵ, and γ are very favourably to those obtained previously by a traveltime inversion (Table 6 in Appendix A). As mentioned previously in the theory section, the estimated ϵ, δ, and γ are the $\epsilon^{(2)}$, $\delta^{(2)}$, and $\gamma^{(3)}$ as in Table 6 in Appendix A.

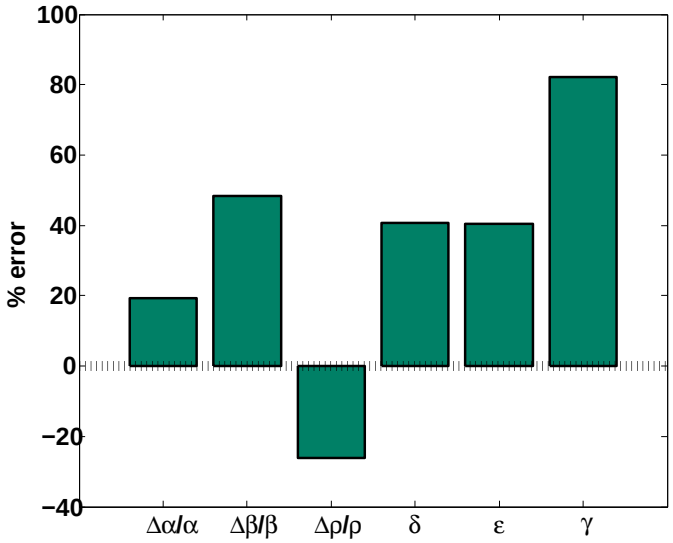

FIG. 16: AVAZ inversion of azimuths 0°, 14°, 27°, 37°, 45°, 53°, 63°, 76°, and 90° for the six parameters $\Delta\alpha/\alpha$, $\Delta\beta/\beta$, $\Delta\rho/\rho$, δ, ϵ, and γ.

CONCLUSIONS

We applied an AVAZ inversion for the Thomsen anisotropy parameters using amplitudes picked from the reflections of an isotropic-HTI interface recorded in a 3D physical model experiment. All three anisotropy parameters ϵ, δ, and γ were successfully estimated, whereby the estimation of the shear-wave splitting parameter from compressional data was of great importance. This AVAZ inversion can be applied to real-world data only if there is enough information about the fractured layer overburden. Also, pre-knowledge of the orientation of the fracture plane is essential in this method.

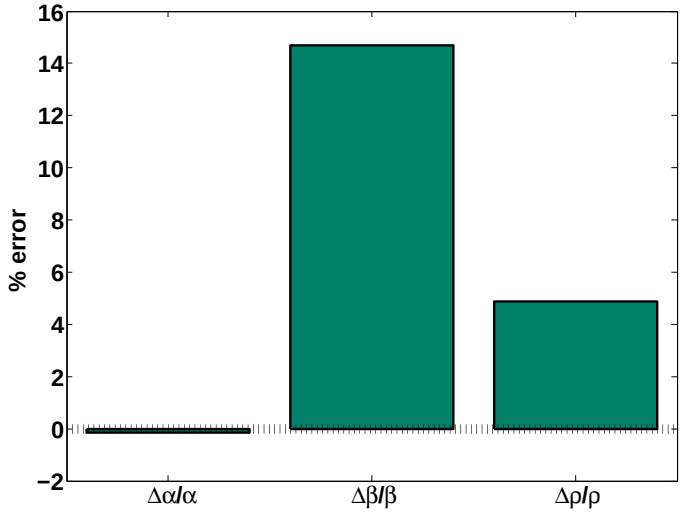

FIG. 17: AVA inversion for $\Delta\alpha/\alpha$, $\Delta\beta/\beta$, and $\Delta\rho/\rho$ from azimuth 90° data.

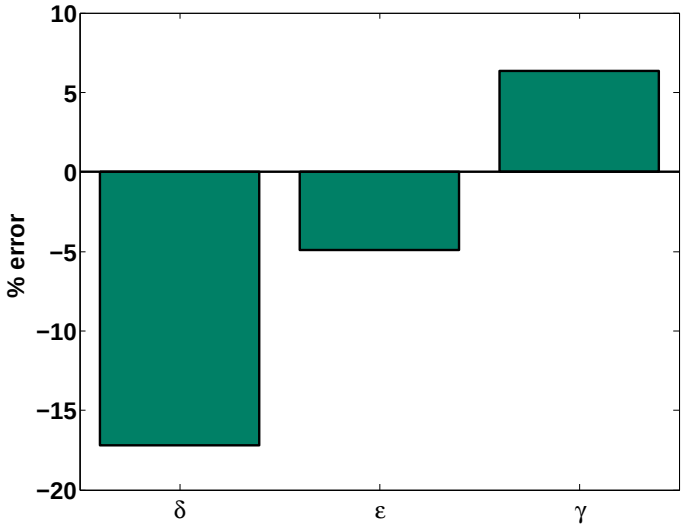

FIG. 18: AVAZ inversion of 0°, 14°, 27°, 37°, 45°, 53°, 63° and 76° for δ, ϵ, and γ using the constraint for $\Delta\alpha/\alpha$, $\Delta\beta/\beta$, and $\Delta\rho/\rho$ from azimuth 90° data.

Although the physical model data are suitable for testing geophysical techniques, they are strongly affected by transducer size issues. We managed to reduce this size effect by shotting the data over the water and using smaller size transducers. We collected physical model data that is suitable for quantitative amplitude analysis, a difficult task that is rarely done so far. The big challenge in the corrections with physical model amplitudes was making the proper corrections for transducer directivity. We coped with this difficulty by calibrating the amplitudes to reflections of the water bottom. The AVAZ inversion simultaneously for six parameters $\Delta\alpha/\alpha$, $\Delta\beta/\beta$, $\Delta\rho/\rho$, ϵ, δ, and γ was unstable because of the small AVA and azimuthal variations in plexiglas-phenolic contrast. A future application of this AVAZ inversion may be more successful if stronger azimuthal or AVA variations is observed.

As our material was very close to being HTI, we didn't use the linear PP reflection coefficients expressions for orthorhombic media for this study. However, the way that we rewrote this equations with the more familiar Thomsen-style anisotropy parameters makes it possible to do this inversion for an orthorhombic layer (more suitable model to express a fractured medium). In an orthorhombic AVAZ inversion, estimation is possible for all six anisotropy parameters ($\delta^{(1)}, \delta^{(2)}, \delta^{(3)}, \epsilon^{(1)}, \delta^{(2)}$, and γ).

We recommend that when doing AVA inversion one should include data from larger incident angles, but not angles close to critical angle. The linear equations are not good approximations near critical angles. Proper inversion of AVA data for both isotropic and anisotropic media near the critical angle must be based on spherical-wave formulations and not plane-wave theory.

ACKNOWLEDGEMENTS

We thank the sponsors of CREWES for their crucial financial support and, in particular, acknowledge the support of the Canadian funding agencies NSERC and MITACS. Dr.s' P.F. Daley, Kris Innanen, John Bancroft, Chad Hogan, Helen Isaac, Rolf Maier, Chuck Ursenbach and Kevin Hall and are greatly acknowledged for their help. Faranak Mahmoudian wishes to thank specially David Henley, David Cho for many constructive discussions.

REFERENCES

Aki, K. and Richards, P. G. (1980). Quantitative seismology: Theory and methods. vol 1.

Alkhalifah, T. (1997). Velocity analysis using nonhyperbolic moveout in transvelsly isotropic media. *Geophysics*, 62:1839–1854.

Bakulin, A., Grechka, V., and Tsvankin, I. (2000). Estimation of frcature paremters from reflection seismic data - part i: Hti model due to single fracture set. *GEOPHYSICS*, (65):1778–1802.

Buddensiek, M. L., m. Krawczyk adn Nina kukowski, C., and Oncken, O. (2009). Performance of piezoelectric transducres in terms of amplitude and waveform. *GEOPHYSICS*, 74(2).

Daley, P. F. and Hron, F. (1977). Reflection and transmission coefficients for transversly isotropic media. *Bull. Seismol. Soc. Am.*, (67):661–675.

Gassaway, G. S. (1984). Effects of shallow reflectors on amplitude versus offset (seismic lithology) analysis. *SEG expanded abstract*, pages 665–669.

Gray, D. (2008). Fracture detection using 3d seismic azimuthal avo. *CSEG RECORDER*, 12:38–49.

Gray, D., Roberts, G., and Head, K. (2002). Recent advances in determination of fracture strike and crack density from p-wave seismic data. *The Leading Edge*, pages 280–285.

Krautkrämer, J. and Krautkrämer, H. (1986). Werkstoffprüfung mit ultrascall. *Springer Verlag*.

Lynn, H. B., Simon, K. M., and Bates, C. R. (1996). Correlation between p-wave avoa and s-wave traveltime anisotropy in a naturally fractured gas reservoir. *The Leading Edge*, (15):931–935.

Mahmoudian, F., Margrave, G., Daley, P. F., Wong, J., and Gallant, E. (2010). Determining elatic constant of an orthorhombic meterial by physicla seismic modeling. *CREWES Report*.

Mallick, S., Craft, K. L., Meister, L. J., and E.Chambers, R. (1998). Determination of the principal directions of azimutha anisotropy from p-wave seismic data. *GEOPHYSICS*, (63):692–706.

Margrave, G. F. (2002). Seimic data processing. *Course notes*.

Nelson, R. A. (2001). Geologic analysis of naturally fractured reservoirs. *CSEG RECORDER*.

Newman, P. (1973). Divergence effects in a layered earth. *Geophysics*, 38:481–488.

Perez, M. A., Grechka, V., and Michelena, R. J. (1999). Fracture detection in a carbonate reservoir using a variety of seismic methods. *GEOPHYSICS*, (64):1266–1276.

Resnik, J. R. (1993). Seismic data processing for avo and ava analysis. *Investigation In Geophysics Series*, (8):175–189.

Rüger, A. (1997). P-wave reflection coefficeints for transversly isotropic models with vertical and horizontal axis of symmetry. *Geophysics*, 62.

Rüger, A. (2001). Reflection coefficeints and azimuthal avo analysis in anisotropic media.

Sava, D. C. and Mavko, G. (2004). Azimuthal analysis of reflectivity for farcture characterization: Rock physics modelling and feild example. *74th Ann. Meeting, Soc. Explo. Geophys. Exp. Abstarcts*.

Schoenberg, M. and Helbig, K. (1997). Orthorhombic media: Modeling elastic wave behavior in a vertically fractured earth. *Geophysics*, 62:1954–1974.

Shuey, R. T. (1985). A simplification of the zoeppritz equations. *GEOPHYSICS*, 50:609–614.

Spratt, R. S., Goins, N. R., and Fitch, T. J. (1993). Pseudo-shear - the analysis of avo. *Investigation In Geophysics Series*, (8):37–56.

Tadeppali, S. V. (1995). 3-d avo analysis: Physical modeling study. *PhD. Thesis, University of Houston*.

Thomson, L. (1988). Reflection seismology over azimuthally anisotropic media. *Geophysics*, 53(3):304–313.

Tsvankin, I. (1997a). Anisotropic parameters and p-wave velocity for orthorhombic media. *Geophysics*, 62:1292–1309.

Tsvankin, I. (1997b). Reflection moveout and parameter estimation for horizontal transverse isotropy. *Geophysics*, 62:614–629.

Tsvankin, I. (2001). Seismic signatures and analysis of reflection coefficients in anisotropic media.

Tsvankin, I. and Grechka, V. (2011). Seismoloigy of azimuthally anisotropic media and seismic fracture characterization.

Ursin, B. (1990). Offset-dependent geometrical spreading in a layered medium. *Geophysics*, 55(4):492–496.

Vavryčuk, V. and Pšenčik, I. (1998). P-wave reflection coefficients in weekly anisotropic elastic media. *Geophysics*, 63(6):2129–2141.

Vestrum, R. W., Lawton, D. C., and Schmid, R. (1999). Imaging structures below dipping ti media. *GEOPHYSICS*, 64.

Wong, J., Hall, K. W., Gallant, E. V., Maier, R., Bertram, M., and Lawton, D. C. (2009). Seismic physical modeling at university of calgary. *CSEG recorder*, 34:36–43.

Wong, J. and Mahmoudian, F. (2011). Physical modeling iii: acquiring physically-modeled data for vvaz/avaz analysis. *CREWES Report*.

APPENDIX A
Elastic constants of utilized material

Our model consists of water, isotropic plexiglas, and orthorhombic phenolic LE material. Density of water, plexiglas and phenolic LE are 1000, 1190, and 1390 kg/m^3, respectively. The P- and S-wave velocity of water and plexiglas are listed in Table 3. For isotropic material, the full density normalized elastic constants matrix can be determined from only compressional and shear velocities; $(A_{ii} = V_P^2, i = 1, 2, 3)$, $(A_{ii} = V_S^2, i = 4, 5, 6)$, and $(A_{ij} = V_P^2 - 2V_S^2, i, j = 1, 2, 3)$.

Table 3: Body wave velocity in water and plexiglas

	P-velocity (m/s)	S-velocity (m/s)
Water	1485	0
Plexiglas	2785	1380

Table 4: Body-waves velocity in phenolic LE

	V_{11}	V_{22}	V_{33}	V_{23}	V_{13}	V_{12}
Velocity (m/s)	2950	3560	3500	1700	1530	1510

Table 5: Density normalized elastic constants of the phenolic LE model. The A_{ij} have the units of $(km/s)^2$.

8.7025	4.9049	4.9626	0	0	0
	12.6736	5.5867	0	0	0
		12.25	0	0	0
			2.89	0	0
				2.3409	0
					2.2801

The phenolic layer in this study is the same as that used by Mahmoudian et al. (2010). All nine density normalized elastic have been determined from P- and S-wave group velocity measurements in arbitrary directions in the three principle planes and the $\pm 45^\circ$ azimuth planes (see Table 5). Note there are minor calculation errors in off-diagonal stiffnesses by Mahmoudian et al. (2010) that have been corrected here. Also, their y-axis is our x_1-axis. The Thomsen-style anisotropy parameters, as explained in the text for the phenolic LE layer, are given in Table 6, which lists the exact forms (used by Rüger)and their linear approximations for the δ parameters (used in renaming the Vavryčuk equation). The linear and exact δ are calculated based on the definitions in Tables 1 and 2 in the text.

APPENDIX B
Deterministic corrections to P-wave reflected amplitudes

As a seismic wave propagates through the earth, its amplitude decays in excess of any AVA effect. In Appendix B we examine decay caused by several non-AVA factors. The decay caused by these factors must be corrected before AVA/AVAZ analysis. can be applied to field reflection data, expect for the source-receiver perceptivity that is specific to physical model data.

Table 6: Anisotropy parameters of phenolic LE layer.

	ϵ	γ	δ (exact)	δ (linear)
$(x_1 - x_3)$ plane	-0.1448	-0.1055	-0.1847	-0.2127
$(x_2 - x_3)$ plane	0.0173	-0.0130	-0.0687	-0.0721
$(x_1 - x_2)$ plane	-0.1567	0.1173	-0.2141	-0.2273

Geometrical spreading

As seismic energy propagates away from a source, the total energy on the wavefront surface stays the same. As the wavefront becomes larger the energy per unit area becomes smaller, and consequently the amplitudes become weaker. This is a geometrical effect and is independent of the medium properties. Consider a seismic ray with amplitude A_1, after traveling the raypath of L the ray amplitude will be A_1/L; so the geometrical spreading factor equals L. Hence, in an AVA study the total ray-path length L is calculated by ray-tracing, and the observed amplitude is multiplied by the geometrical spreading L do remove the amplitude decay due to spreading. This is be the exact correction for geometrical spreading, which is not always possible. There is a readily applied correction for geometrical spreading by a zero-offset correction. The zero-offset geometrical correction is (Resnik, 1993)

$$g_0(t) = V_{rms}^2 t, \tag{1}$$

where t is two way traveltime and V_{rms} is an estimate of the root-mean-square (rms) velocity at the corresponding zero-offset traveltime; each trace is multiplied by zero-offset correction. This simple correction derives from an analysis of spreading in the vicinity of the zero-offset in a horizontally layered medium by Newman (1973). This correction does not necessarily compensate for spreading at far offsets. There is an offset-dependent geometrical spreading correction by Ursin (1990) as

$$g_1^2(t) = g_0^2(t) + \left[2\left(\frac{V_{rms}}{V_1}\right)^2 - 1\right] x^2 + \frac{1}{t^2}\left(\frac{1}{V_1^2} - \frac{1}{V_{rms}^2}\right) x^4, \tag{2}$$

where x is source-receiver offset, and V_1 is the first layer velocity. The geometrical spreading correction is applied to reflection data before move-out as a gain function at the two-way-time t.

In this study we used raytracing through isotropic horizontal layers for the calculation of the geometrical spreading correction. Figure 19 shows the water-plexiglas reflector amplitudes from azimuth 0° data (from the four-layered model) versus incident angle that have been corrected for geometrical spreading by raytracing, zero-offset, and offset-dependent gain; the corrected amplitudes has been compared to theoretical Zoeppritz predicted P-wave reflectivities. The theoretical predicted P-wave reflectivity has been calculated using both plane-wave and spherical waves in the Zoeppritz solver (available in CREWES Matlab toolbox).

Emergence angle

A vertical-component geophone only detects the vertical component of the total motion, whereas in AVA analysis the total motion is needed which correctly represent the actual reflectivity. The total motion can be calculated from vertical recordings knowing the emergence angle. For the angle of emergence, θ, measured from the vertical. The total motion is

$$Total\ motion = \frac{vertical\ recording}{\cos\theta}. \tag{3}$$

The emergence angle can be calculated using raytracing or modeling using an estimated of overburden velocity model. See Figure 8 for the emergence angle correction applied to the water-plexiglass reflector amplitudes picked from azimuth 0° data with transducer's tip are $2mm$ beneath the surface of the water. Each correction brings the amplitudes closer to the theoretically Zoeppritz predicted amplitudes.

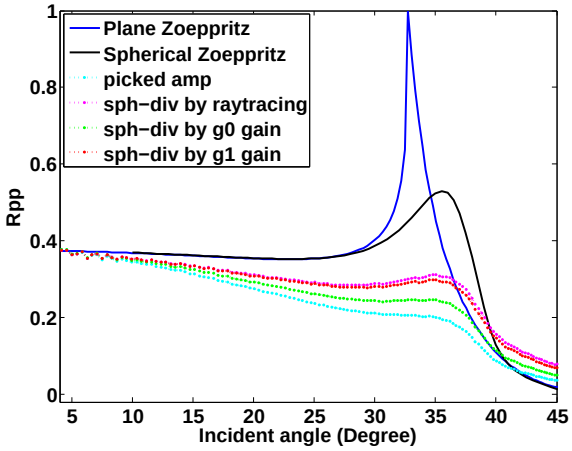

FIG. 19: Azimuth 0° data: geometrical correction for amplitudes picked from the first reflector of the four-layered model data. The amplitudes have been compared to Zoeppritz predicated reflection coefficients. The offset-dependent g_1 compensates nearly as good as the exact raytracing geometrical correction.

Free surface

The ground or water surface is a free surface since the stress becomes zero at such a boundary. Seismic waves reflected off the free surface, and both incident reflected waves are recorded by geophones at the free-surface. If we want only the amplitude of the reflected from the bottom layers, the reflected wave from the free surface must be taken out (see Figure 20). The vertical component detected at the free surface:

$$Z = \widehat{I}(1 - R_{0pp})\cos\theta_0 + R_{0ps}\sin\theta_{0S}, \tag{4}$$

where $\widehat{I}$ is the P-incident amplitude, and R_{0pp} and R_{0ps} are the free-surface PP and PS reflection coefficient respectively. Knowing the emergence angle θ, the incident amplitude $\widehat{I}$ can be calculated from vertical recording Z. It is evident that with the free-surface correction, the emergence angle correction above is not needed; however, when receivers are deep in the water, the detected event does not have a free-surface reflection, and so do not need a free-surface correction. Only the emergence angle correction is needed in this case.

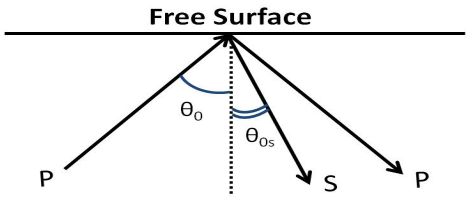

FIG. 20: Free surface boundary condition (courtesy of Spratt et al. (1993)).

Transmission loss

Consider a two-layer model as in Figure 21; the recorded amplitude from the second layer reflector is $T_1 R_2 T_1'$. Assuming that the recoded amplitude represents the reflectivity R_2 the effect of $T_1 T_1'$, which is called "transmission loss", should be removed. Knowing an estimate of the overburden velocity model, the transmission loss factor can be determined. However, in reality a deterministic correction for transmission loss is problematic as the overburden can not be perfectly characterized. Gassaway (1984) states that the transmission loss is the most significant problem encountered in AVO analysis. In practice the transmission loss is compensated using a statistical correction as described below in the section on residual amplitude compensation. In this study, knowing the overburden of water and plexiglass, we determined the transmission loss effecting the plexiglas-phenolic reflector amplitudes.

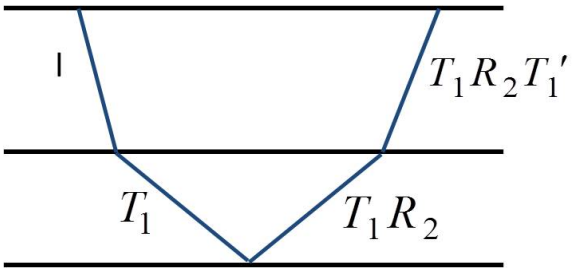

FIG. 21: Transmission loss effect in a two-layer model. The initial amplitude is 1, T_1 is the transmission coefficient going from layer 1 to layer 2, R_2 is the reflection coefficient from layer 2, and T_1' is the transmission coefficient going from layer 2 to layer 1. The transmission loss factor is $T_1 \times T_1'$.

Anelastic attenuation

Attenuation will also effect the AVA behavior of recorded reflections. For a constant Q, Spratt et al. (1993) states that the amplitude A will decay according to

$$A \sim A_0 \left\{ 1 - \left(\frac{\pi f t}{Q} \right) \frac{V^{(2)}}{V_P^2} \sin^2\theta \right\}, \tag{5}$$

where A_0 is the unattenuated amplitude, f is the frequency, θ is the incident angle, V_P is the P-velocity, and $V^{(2)} = \frac{1}{t}\int_0^t V_P^2(\acute{t})d\acute{t}$ with t' the one-way traveltime; in this correction only one frequency the dominant frequency, is considered. The simple industry practiced attenuation correction is $\exp(\alpha t)$, where α is a constant with value close to one, and t in two-way traveltime. In this study, we did not use any attenuation correction as our layers are considered to be non-attenuating.

Array effect

The use of arrays of sources and receivers is commonplace in field acquisitions. The response of each receiver (or source) is summed up and recorded as the total array response. The array response does not exactly represent any of the amplitudes recorded by each of the receivers. The response of a linear array of length L is given by

$$R(\theta) = \frac{\sin\left(\frac{\pi L}{\lambda}\sin\theta\right)}{\left(\frac{\pi L}{\lambda}\sin\theta\right)}, \tag{6}$$

where λ is the wavelength; therefore, a linear array can have a frequency-dependent effect. Spratt et al. (1993) gives practical array effect corrections for land recordings. In the physical modeling experiment used in this study we did not have source (or receiver) arrays, however the transducers can be treated as a finite-size array of point sources spaced closely together. The total effective response can be calculated and used as a transducer directivity correction for physical model data; a detailed analysis of this method is available in Wong and Mahmoudian (2011).

Scaling

In a seismic experiment, the source wavelet is convolved with the earth's reflectivity to produce seismic data. After all the above corrections have been made to the data, the last step in the deterministic extraction of reflectivity from seismic data, involves deconvolving the source wavelet from the data. The deconvolved data still needs a scaling factor to bring the magnitude of the amplitudes into the range of $[-1, 1]$. Such a scaling problem is caused by filtering at the several processing steps, even in a true-amplitude processing flow. So the data should be deconvolved and also denoised. Coherent noise (such as surface waves) would ruin an AVA analysis. For denoised data, the convolutinal model is

$$S(t) = w(t) * R(t), \tag{7}$$

where $S(t)$ is a seismic trace, $W(t)$ is the wavelet, and $R(t)$ is the reflectivity. Ideally, after the deconvolution, the deconvolved data will be a scaled version of the reflectivity $S(t) \cong aR(t)$, where a is a scaler. We seek

a value of this scaler before the AVA analysis and follow (Margrave, 2002) in deriving such a scaler. This means minimizing $\Phi(t) = S(t) - aR(t)$ in a least-squares sense to derive the scaler a. In discrete form $S_j = aR_i$ and $\Phi_j = S_j - aR_j$, then minimizing Φ means

$$\vartheta = \sum_{j=0}^{\max} \left(S_i - aR_j\right)^2 = \min, \tag{8}$$

then $\frac{\partial \vartheta}{\partial a} = \sum_j -2R_j \left(S_j - aR_j\right) = 0$, and the scaler will be:

$$a = \frac{\sum_j R_j S_j}{\sum_j R_j R_j}, \tag{9}$$

where the $\sum_j R_j S_j$ is the zero-lag crosscorrelation of $R(t)$ and $S(t)$, and $\sum_j R_j R_j$ is the zero-lag autocorrelation of $R(t)$. This single scalar will be applied to the whole data.

Residual amplitude compensation

Finding the scalar above completes our discussion on deterministic amplitude corrections. However, in practise the deterministic corrections are never ideal, and there might be some residual corrections left. The residual corrections are done using statistical methods. Resnik (1993) describes the residual amplitude compensation as removing the average variation of amplitude from the data, where the average was measured in a series of overlapping 400 ms time windows across the entire line. After residual amplitude compensation, the average amplitude variation is diminished, though local AVA anomalies are still intact. This note on residual compensation is presented so that our discussion on the amplitude corrections in general will be complete; however, we did not apply any statistical corrections to the physical model data.